MOX-Report No. 34/2019

Three-dimensional physics-based earthquake ground motion simulations for seismic risk assessment in densely populated urban areas

Antonietti, P. F.; Mazzieri, I.; Melas, L.; Paolucci, R.;

Quarteroni, A.; Smerzini, C.; Stupazzini, M.

THREE-DIMENSIONAL PHYSICS-BASED EARTHQUAKE GROUND MOTION SIMULATIONS FOR SEISMIC RISK ASSESSMENT IN DENSELY POPULATED URBAN AREAS

P. F. Antonietti[1], I. Mazzieri[1], L. Melas[1], R. Paolucci[2],
A. Quarteroni[1,3], C. Smerzini[2] and M. Stupazzini[4]

[1] MOX – Laboratory for Modelling and Scientific Computing, Department of Mathematics,
Politecnico di Milano, Piazza L. da Vinci *32*, *20133* Milano, Italy
`paola.antonietti@polimi.it, ilario.mazzieri@polimi.it,`
`laura.melas@polimi.it, alfio.quarteroni@polimi.it`
[2] Department of Civil and Environmental Engineering, Politecnico di Milano, Piazza L. da
Vinci *32*, *20133* Milano, Italy
`roberto.paolucci@polimi.it, chiara.smerzini@polimi.it`
[3] Chair of Modeling and Scientific Computing (CMCS), Mathematics Institute of
Computational Science and Engineering (MATHICSE), École Polytechnique Fédérale de
Lausanne (EPFL), Station *8*, *1015* Lausanne, Switzerland
[4] Munich RE, Geo Risks Königinstr. *107*, *80802* Munich, Germany
`MStupazzini@munichre.com`

Keywords: computational seismology – earthquake ground motions – numerical modelling – wave propagation.

Abstract

In this paper we introduce a mathematical and numerical approach aiming at coupling the physically simulated ground motion caused by earthquakes with empirical fragility functions introduced to model the structural damages induced to buildings. To simulate earthquake ground motion we solve a three-dimensional differential model at regional scale describing the propagation of seismic waves through the earth layers up to the surface, based on employing the discontinuous Galerkin spectral element method; selected intensity measure, retrieved from the synthetic time histories, are then employed as input for a vulnerability model based

---

[9] The first, second and third authors have been partially supported by SIR starting grant `n.n. RBSI14VT0S` funded by MIUR - Italian Ministry of Education, Universities and Research.

on fragility functions, in order to obtain a reliable prediction of buildings damage state. The main features and effectiveness of the proposed numerical approach are tested on the Beijing metropolitan area (China).

1 Introduction

In the last few decades, losses induced by natural disasters have shown a dramatic increase on a worldwide scale. The reasons are manifold and include the increase in world population, together with the development of new mega-cities with population larger than 2 millions, as well as the development of highly exposed regions and high vulnerability of modern societies and technologies [77]. Many of these densely populated areas are located in seismic prone areas. The destructive earthquakes of the last decade, such as Chile (Haiti 2010), New Zealand (Canterbury 2010 - 2011), Japan (Tohoku 2011, Kunamoto 2016) and Italy (L'Aquila 2009, Po Plain 2012, Norcia 2016), have caused a very high number of victims with losses estimated of the order of several billion dollars. For example, the Haiti earthquake (2010) counts 159.000 fatalities, whereas the overall economic losses caused by the Tohoku 2011 earthquake were estimated to be about 210 billion US dollars with about 15.500 victims (`https://natcatservice.munichre.com`).

The assessment of seismic risk at portfolio, urban or regional scale is a key element for the definition of risk mitigation strategies to lessen the adverse economic and social effects of earthquakes, the planning and management of emergency response in the aftermath of a disaster event and for the definition of earthquake insurance schemes for risk transfer objectives. A variety of methodologies, tools and applications dealing with different components of seismic risk assessment have been proposed, see, e.g., the overview in [34]. In general, the chain of seismic risk assessment involves first the quantification of seismic hazard, then its combination with suitable vulnerability models of structures and facilities and, finally, the measurement of expected losses by incorporating the exposure information. Seismic hazard models provide a quantification of the expected earthquake shaking in a given area in terms of various ground motion Intensity Measure (IM), such as Peak Ground Acceleration (PGA) or acceleration response spectra ordinates (SA). For a structural typology, the direct physical damage can be determined using suitable fragility/vulnerability relationships providing the probability of damage/loss, conditioned on the level of IM. Eventually, economic (direct and indirect) and social (casualties) losses can be estimated as a function of physical damage estimates.

In this paper we focus on the main challenges arising from the characterization of earthquake ground motion, that is a crucial step in seismic hazard analysis having the goal of providing estimates of the probability distribution of ground motion IM as a function of explanatory variables, such as magnitude, source-to-site distance and site conditions, amongst others. An extensive body of approaches exists for this purpose, ranging from Ground Motion Prediction Equations (GMPEs), Empirical Green Functions and stochastic methods, to three-dimensional (3D) numerical simulations, see review in [30]. These approaches differ essentially for the amount and detail of input information, as regards both the seismic source and propagation path from the source to the site, and the levels of output, either in terms of peak values of ground motion or an entire time history.

GMPEs are statistical regressions on instrumental observations from past earthquakes and represent the most commonly used approach for ground motion prediction, especially in engineering practice, see [31]. Nonetheless, the GMPEs suffer from some major limitations, especially when used for earthquake ground motion prediction at urban or regional scale. First, they are poorly calibrated in the near-source region of moderate to large earthquakes, i.e. in the range of distance-magnitude which typically dominate the hazard for many cities worldwide [62]. Second, as a consequence of ergodic assumption [2], they cannot account for region-, path- and site- specific effects related to the earthquake source, recording site conditions (e.g. complex site effects in case of large sedimentary basins, where many megacities in the world are built) and source-to-site path. Third, GMPEs alone cannot provide reliable estimates of the spatial correlation of ground motion, which may be crucial for seismic risk assessment of large urban areas with spatially distributed portfolios or infrastructural systems, see e.g., [45, 61, 83].

In recent years, boosted by the continuous development of advanced numerical methods together with computational power facilities, there has been an increasing research of numerical modeling for the simulation of seismic wave propagation phenomena [11, 6] so that 3D physics-based simulations (referred to as PBS hereafter) have emerged as a powerful and effective tool for earthquake ground motion prediction [18]. Typically they are based on finite difference (FD) methods, finite element (FE) methods and spectral element (SE) methods that solve the discretization of the elastodynamics equation [40, 53, 36, 49]. Therefore, the output of PBS consists of ground motion time histories reflecting the physics of the seismic wave propagation problem as a whole, from the fault rupture to the propagation path and local site response. The SE approach is among the most popular methods in computational seismology due to its capability of providing highly accurate solutions. In [12] Discontinuous Galerkin SE (DGSE) methods have been proposed and analyzed to further enhance the flexibility of SE methods, see also [47, 7, 9, 55, 10, 4, 5]. Indeed, DGSE methods are well suited for capturing local variations of the physical solution since they preserve the same accuracy of SE approaches and keep the numerical dispersion and dissipation errors low. Moreover, they are more flexible than SE methods, because they allow for non-conforming grids and locally varying local approximation degrees in the numerical model [12, 7].

In recent years, PBSs have achieved a substantial maturity in the scientific community, so that they can now be embedded within simulation-based seismic hazard assessment frameworks [39, 81, 18, 58, 44, 79] and in the generation of large scale simulation-based seismic risk assessments [63, 26, 27, 75]. Use of PBS for seismic risk assessments are still rather uncommon even in research developments. The HayWired Earthquake scenario [26, 27] is an example of cutting-edge evaluation of scenario-based seismic risk from 3D simulations: the physics-based ground shaking scenario of a hypothetical M_w 7 earthquake on the Hayward Fault (San Francisco Bay area, California) was the basis to estimate in a comprehensive framework the expected physical and environmental damages resulting not only from the earthquake shaking but also from cascading events (such as liquefaction, landslide, afterslip) and to provide insights into recovery and restoration of structures and lifelines, social and economic consequences, planning of emergency responses and policy considerations. Recently, Smerzini and Pitilakis [75] combined 3D physics-based simulations with the capacity spectrum method to estimate the damage to RC buildings in the city of Thessaloniki during the destructive M_w 6.5 1978 earthquake and to compare it with available post-earthquake damage observations.

In this paper we make a step forward in the development of PBS-based seismic risk assessment in large urban areas. We propose a workflow for seismic risk assessment to yield improved seismic damage scenarios, which couples, on one side, a rigorous numerical model for the prediction of near-source earthquake ground motion with, on the other side, suitable fragility functions for prescribed building typologies. 3D physics-based earthquake scenarios, that are the key ingredient for the proposed workflow, are constructed employing the DGSE method proposed in [12] and implemented in the open source code SPEED (`http://speed.mox.polimi.it`, cf. also [55]). Replacing standard GMPEs with PBSs is, in fact, expected to provide more accurate, site-specific estimates of earthquake ground motion and, then, of the resulting damage, especially in such conditions where coupling of near-field effects and complex site amplification in sedimentary basins may play a key role. Since our aim is to improve the capability of realistically modelling the ground shaking, the results discussed in this paper can be incorporated within both deterministic and probabilistic frameworks for hazard and risk assessment.

The paper is organized as follows. In Section 2 the proposed workflow for seismic risk assessment combining PBSs scenarios with fragility models is presented. The theoretical and numerical framework at the basis of the two main components of this workflow, i.e., the DGSEM for physics-based numerical simulation of earthquakes and the fragility functions for the vulnerability model, are discussed in Sections 3 and 4, respectively. Finally, in Sections 5 and 6, we present an application case study dealing with the large metropolitan area of Beijing (China). The city of Beijing is located in the proximity of a well-known mapped fault system capable of triggering severe earthquakes of magnitude up to 7.3. Maps of seismic damage are produced with reference to the specific class of high-rise buildings, accounting for a rather wide set of fault rupture realizations with magnitude in the range 6.5-7.3.

2 Seismic risk assessment via 3D physics-based numerical simulations: workflow

For a specific asset, seismic risk is computed by convolution of hazard with vulnerability. Conventionally, the probability of damage is estimated on the basis of the total probability theorem, as follows:

$$P(DS \geq d_s) = \int P(DS \geq d_s|IM) f_{IM}(\mathtt{im})\, d\mathtt{im} \tag{1}$$

where $P(DS \geq d_s|IM)$ represents the probability of exceeding a certain damage level (or state) conditioned on the intensity measure IM, i.e., the fragility function expressing the complementary cumulative distribution function for DS conditional to IM, while $f_{IM}(\mathtt{im})$ is the probability density function of the given IM. In the most comprehensive context of performance-based earthquake engineering, $f_{IM}(\mathtt{im})$ is derived from the seismic hazard curve at a site (giving the annual probability of exceedance as a function of the given IM) computed through a Probabilistic Seismic Hazard Assessment (PSHA), and Equation (1) allows to compute the annual probability of exceedance of a given loss metric (e.g. monetary losses or damage state, the latter being related to losses through correlations of damage with repair or replacement costs). In deterministic risk calculations, the risk is computed for a single ground shaking scenario without computing the convolution integral of Equation (1). Regardless of the approach considered, estimation of IM, both within a probabilistic or deterministic framework, is generally computed through GMPEs with the limitations previously discussed in the Introduction.

The key element of the workflow proposed in this paper (see Figure 1 for a schematic representation) is the characterization of seismic ground shaking and of its spatial variability through 3D physics-based numerical models of earthquakes. These earthquake scenarios are based on solving approximately a differential problem modeling the displacement of a (visco)elastic medium subjected to an external excitation source. The numerical method employed to approximate the displacement field is the DGSE method proposed in [12] and implemented in the open source code SPEED (`http://speed.mox.polimi.it`, cf. also [55]). Besides being verified in a number of benchmarks, see [55, 9, 10], SPEED has been proven successful to simulate real earthquakes, such as the 2009 April 6th L'Aquila, Central Italy [35], the 2011 February 22nd Christchurch, New Zealand [42], the 2012 May 29th Po Plain, Northern Italy [59], the 1978 June 20th Volvi, Northern Greece [76], the 1915 January 15th Marsica [57].

Each numerical simulation provides as output, at any site of interest, the full waveform of ground motion compatible with the source rupture process (causative fault, magnitude M_w, hypocenter location, fault slip distribution, etc..), the source-to-site path and the local geological conditions. Note that, for a given magnitude M_w, multiple realizations are simulated to account for the aleatory uncertainty associated with the fault rupture process, in terms of slip distribution, hypocenter location and other kinematic source parameters (e.g. rupture velocity and rise time). For sake of clarity, in the following the term *scenario* will be used to refer to a set of earthquakes on a given fault characterized by a prescribed magnitude M_w, while *footprint* is used to denote the specific realization (i.e. in terms of co-seismic slip distribution across the fault and hypocenter location) within a given scenario. From the synthetic waveform, any ground motion IM can be computed, depending on the class of structures/infrastructures at risk, provided that the simulated ground motion is *broadband*, i.e., it is sufficiently accurate in a broad frequency range of interest for the seismic response of structures. Once the selected IM is computed, it is used as input to the fragility functions for the target class of structures to compute the probability of exceedance of a given damage state.

The workflow implemented in this work allows one to compute seismic risk estimates at two different levels. At the first level ($L1$), deterministic seismic risk estimates, i.e. $P(DS \geq d_s|IM)$, are provided for representative earthquake footprints computed through a single numerical simulation. At the second level ($L2$), based on

Equation (1), seismic risk estimates are computed for a given earthquake scenario with prescribed magnitude M_w, i.e. $P(DS \geq d_s | scenario)$, exploiting a statistically significant set of earthquake footprints, from which the probability distribution of ground motion can be computed. This implies that, for any site of interest, the probability distribution of earthquake shaking, i.e., the term $f_{IM}(\mathtt{im})$ of the aforementioned equation, which is typically given by GMPEs, can be computed from the N footprints of the given earthquake scenario. For the latter approach, in order to evaluate $P(DS \geq d_s)$, we have to compute the integral in Equation (1). For the sake of accuracy, we adopt the Gaussian quadrature formula, especially for the evaluation of low and very low probabilities associated with rare events, e.g. collapse of structures. Note that under specific hypothesis it is possible to calculate analytically the value of the integral in Equation (1). In our case, for the mathematical description of $P(DS \geq d_s | IM)$ we refer to Section 4 (see Eq. (9)), whereas we assume that IM is log-normally distributed with probability density function given by

$$f_{IM}(\mathtt{im}) = \frac{1}{\mathtt{im}} \frac{1}{\sigma_{im}\sqrt{2\pi}} \exp\left(-\frac{1}{2\sigma_{im}^2} \left(\ln \frac{\mathtt{im}}{\mu_{im}} \right)^2 \right), \tag{2}$$

where μ_{im} and σ_{im} are the median and logarithmic standard deviation.

In our study, we are mainly interested in the methodological chain for seismic risk assessment via PBS, so that we do not explicitly account for specific exposure models of the region under study. This means that, as output, we provide risk estimates for any site of the model which may hypothetically contain a prescribed building typology. Furthermore, only physical damage predictions are provided, overlooking the computation of economic and/or social losses. In the two following sections we will focus our attention on the two main ingredients of the workflow of Figure 1, i.e., on one hand a rigorous numerical model for the prediction of near-source earthquake ground motion (Section 3) and on the other hand suitable fragility functions for prescribed building typologies (Section 4).

3 DGSE methods for ground motion prediction

Our mathematical model for earthquake scenarios consists in the dynamic equation in a portion of soil that we identify (at rest) with the three-dimensional region $\Omega \subset \mathbb{R}^3$ in the temporal interval $(0, T]$. The linear momentum equation is given by

$$\rho \ddot{\mathbf{u}} + 2\rho\xi\dot{\mathbf{u}} - \nabla \cdot \boldsymbol{\sigma} + \rho\xi^2\mathbf{u} = \mathbf{f} \quad \text{in } \Omega \times (0, T], \tag{3}$$

where ρ is the medium density, ξ is a suitable decay factor proportional to the inverse of time, $\mathbf{u}$ is the unknown displacement field, $\boldsymbol{\sigma}$ is the stress tensor and $\mathbf{f}$ represents the seismic source. Here $t = 0$ conventionally represents the time instant of the earthquake origin. To simplify the notation, we implicitly assume the dependency in space and time of the quantities $\mathbf{u}$, $\boldsymbol{\sigma}$ and $\mathbf{f}$, whereas ρ and ξ only have the space dependency. Equation (3) is supplemented with a constitutive relation that express the stress tensor as a function of the displacement. Here, we consider the Hooke's law, i.e.,

$$\boldsymbol{\sigma} = \mathcal{D}(\lambda, \mu) : \boldsymbol{\varepsilon}(\mathbf{u}) \qquad \text{in } \Omega \times (0, T], \tag{4}$$

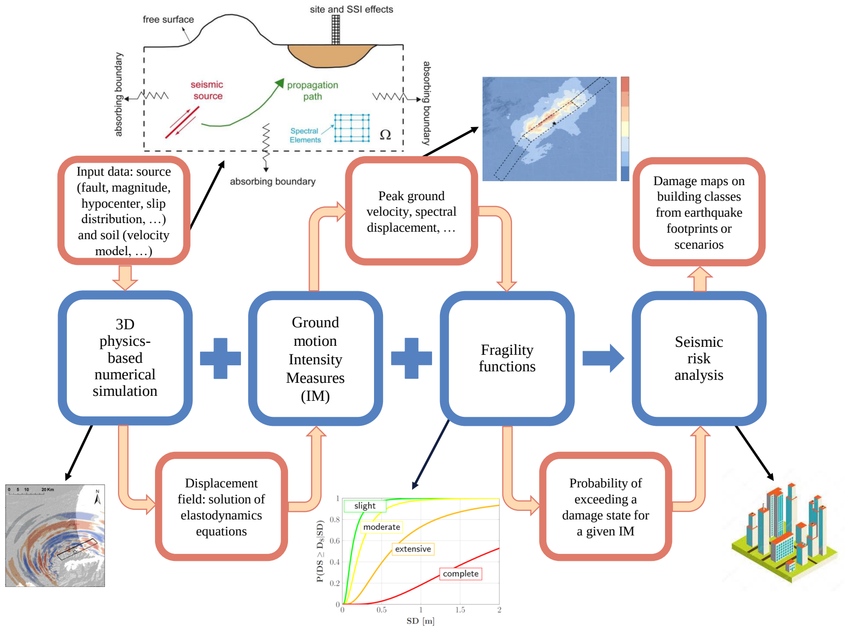

Figure 1: Workflow for seismic risk assessment based on 3D PBS.

where $\mathcal{D}$ is a fourth-order tensor encoding the material properties of the medium depending on the first and second Lamé parameters λ and μ, $\boldsymbol{\varepsilon}$ is the symmetric gradient, and the symbol : denotes a contraction over adjacent indexes. Finally, boundary conditions (such as the free-surface conditions), along with initial conditions, are prescribed in (3)–(4) in order to obtain a well-posed problem. Boundary and initial conditions can take the form

$$\boldsymbol{\sigma}\mathbf{n}_{|\partial\Omega} = \mathbf{t}, \quad \mathbf{u}_{|t=0} = \mathbf{u}_0, \quad \dot{\mathbf{u}}_{|t=0} = \mathbf{u}_1, \tag{5}$$

respectively, where $\mathbf{t}$, $\mathbf{u}_0$ and $\mathbf{u}_1$ represent given traction, displacement and velocity fields, respectively and $\mathbf{n}$ is the outward pointing normal vector from the boundary of the domain $\partial\Omega$. In order to model transparent boundaries, a suitable modification of the traction $\mathbf{t}$ field is considered on the artificial boundaries, see [78, 8]. Hereafter, we will use the symbols v_p and v_s to denote the characteristic compressional and shear wave speeds of the medium, defined as $v_p = \sqrt{(\lambda + 2\mu)/\rho}$ and $v_s = \sqrt{\mu/\rho}$.

The seismic source $\mathbf{f}$ in (3) is described through a kinematic finite-fault model expressed in terms of a distribution of double-couple point sources. Its mathematical representation is based on the seismic moment tensor $m(\mathbf{x}, t)$ defined for $0 \leq t < T$ as in [1],

$$m_{ij}(\mathbf{x}, t) = \frac{M_0(\mathbf{x}, t)}{V}(s_i\nu_j + s_j\nu_i), \quad i, j = 1, \ldots, 3,$$

where $\boldsymbol{\nu}$ and $\mathbf{s}$ are the fault normal and the unit slip vector along the fault, respectively. $M_0(\mathbf{x}, t)$ is the time history of the moment release at the source point $\mathbf{x}$ inside the elementary volume V. Finally, the body force distribution $\mathbf{f}$ is given by the relation $\mathbf{f}(\mathbf{x},t) = -\nabla \cdot m(\mathbf{x},t)$, cf. [36]. Following [12], see [8] for a review, we introduce the DGSE space discretization to problem (3)–(5) based on a domain decomposition approach. We start by a discretization of the spatial differential operators in (3)–(5) that relies on a time-independent spatial decomposition of the domain Ω, as follows. At the first level, we subdivide Ω into K non-overlapping regions Ω_k, $k = 1,\dots,K$, such that $\Omega = \cup_{k=1}^{K}\Omega_k$, and we denote by $\mathcal{S}$ the collection of the interfaces between subdomains. Note that this (macro) decomposition can be geometrically non-conforming. Then problem (1) is solved in each Ω_k together with transmission conditions at the the interface between the sub-domains that are encoded in the scheme. Then, within each subdomain Ω_k, we construct a grid $\mathcal{T}_{h_k}$ made of hexahedral elements E, with diameter h_E, and assign a polynomial approximation degree $N_k \geq 1$. Notice that mesh generation is performed independently on each subdomain and also the local polynomial degree N_k can vary subdomainwise. We define $\mathcal{T}_h$ to be the union of the (independently generated) grids $\mathcal{T}_{h_k}$, and collect all the element faces (here a face is the non empty interior of the intersection of two neighboring hexahedral elements that belong to $\mathcal{T}_h$) that lie on the interface $\mathcal{S}$ in the set $\mathcal{F}_h$. Problem (3)–(5) is then discretized on each subdomain Ω_k with a SEM of degree N_k and at the interfaces $\mathcal{F}_h$ the DG paradigm is employed. Then, denoting by $\mathbf{V}_{DG}$ the discrete space of function that are piecewise continuous polynomials of degree N_k in each coordinate direction on each subdomain Ω_k, and that can be discontinuous at the interface $\mathcal{S}$, the semi-discrete DGSEM reads as follows: for any $t \in (0,T]$, find $\mathbf{u}_h = \mathbf{u}_h(t) \in \mathbf{V}_{DG}$ such that

$$\int_\Omega \rho \ddot{\mathbf{u}}_h \cdot \mathbf{v}\, d\mathbf{x} + \int_\Omega 2\rho\xi \dot{\mathbf{u}}_h \cdot \mathbf{v}\, d\mathbf{x} + \mathcal{A}_h(\mathbf{u}_h,\mathbf{v}) = \int_\Omega \mathbf{f}(t)\cdot \mathbf{v}\, d\mathbf{x} + \int_{\partial\Omega} \mathbf{t}(t)\cdot\mathbf{v}\, d\mathbf{s}, \quad (6)$$

for any $\mathbf{v} \in \mathbf{V}_{DG}$, where

$$\begin{aligned}\mathcal{A}_h(\mathbf{u},\mathbf{v}) = &\sum_{E\in\mathcal{T}_h} \left(\int_E \boldsymbol{\sigma}(\mathbf{u}) : \boldsymbol{\varepsilon}(\mathbf{v})\, d\mathbf{x} + \int_E \rho\xi^2 \mathbf{u}\cdot\mathbf{v}\, d\mathbf{x} \right) \\ &+ \sum_{F\in\mathcal{F}_h} \left(-\int_F \{\boldsymbol{\sigma}(\mathbf{u})\} : [\![\mathbf{v}]\!]\, d\mathbf{s} - \int_F [\![\mathbf{u}]\!] : \{\boldsymbol{\sigma}(\mathbf{v})\}\, d\mathbf{s} + \int_F \eta_F [\![\mathbf{u}]\!] : [\![\mathbf{v}]\!]\, d\mathbf{s} \right).\end{aligned}$$

Here, we use the standard notation for the definition of jump $[\![\cdot]\!]$ and average $\{\cdot\}$ operators, see, e.g. [8]. On each face $F \in \mathcal{F}_h$ shared by two elements $E^+ \subset \Omega_{k^+}$ and $E^+ \subset \Omega_{k^-}$ the penalty parameter η_F is defined as

$$\eta_F = \alpha\{\mathcal{D}\}_A \frac{\mathtt{N}^2}{\mathtt{h}},$$

where $\{\cdot\}_A$ is the harmonic average of the quantity q across F, α is a (large enough) positive constant to be properly chosen [14, 15, 33], and $\mathtt{N}$ and $\mathtt{h}$ are defined on each face $F \in \mathcal{F}_h$ as $\mathtt{N} = \max\{N_{k^+}, N_{k^-}\}$ and $\mathtt{h} = \min\{h_{k^+}, h_{k^-}\}$. Error bounds and stability estimates for problem (6) can be found for instance in [68, 67, 12, 7, 9, 10]. The algebraic version of (6) can be obtained by: (i) introducing a basis $\{\boldsymbol{\Psi}\}_{i=1,\dots,N_h}$ for the finite element space $\mathbf{V}_{DG}$; (ii) expressing $\mathbf{u} \in \mathbf{V}_{DG}$ as linear combination of the shape functions, i.e. $\mathbf{u}(\mathbf{x},t) = \sum_{i=1}^{N_h} \mathsf{U}_j(t)\boldsymbol{\Psi}_j(\mathbf{x})$; and (iii) choosing $\mathbf{v} = \boldsymbol{\Psi}_i$ in for any $i = 1,...,N_h$. The resulting system has the following structure

$$\mathsf{M}\ddot{\mathsf{U}}(t) + \mathsf{C}\dot{\mathsf{U}}(t) + \mathsf{A}\mathsf{U}(t) = \mathsf{F}(t), \quad t \in (0,T], \tag{7}$$

together with initial conditions $\mathsf{U}(0) = \hat{\mathbf{u}}_0$ and $\dot{\mathsf{U}}(0) = \hat{\mathbf{u}}_1$, being $\hat{\mathbf{u}}_0$ and $\hat{\mathbf{u}}_1$ suitable approximation in $\mathbf{V}_{DG}$ of the initial data $\mathbf{u}_0$ and $\mathbf{u}_1$. In (7), the vector $\mathsf{U}(t) \in \mathbb{R}^{N_h}$ contains the unknown expansion coefficients in the chose basis, i.e. $\mathsf{U}_j(t) = \mathbf{u}(\mathbf{x}_j,t)$. The mass, damping, and stiffness matrices M, C and A are defined as

$$\begin{aligned}
\mathsf{M}_{ij} &= \int_\Omega \rho\boldsymbol{\Psi}_j \cdot \boldsymbol{\Psi}_i \, d\mathbf{x}, && i,j = 1,...,N_h,\\
\mathsf{C}_{ij} &= \int_\Omega 2\rho\xi\boldsymbol{\Psi}_j \cdot \boldsymbol{\Psi}_i \, d\mathbf{x}, && i,j = 1,...,N_h\\
\mathsf{A}_{ij} &= \mathcal{A}_h(\boldsymbol{\Psi}_j, \boldsymbol{\Psi}_i), && i,j = 1,...,N_h,
\end{aligned}$$

respectively. Finally, the right-hand side $\mathsf{F}(t)$ has the following expression

$$\mathsf{F}_i(t) = \int_\Omega \mathbf{f}(t) \cdot \boldsymbol{\Psi}_i \, d\mathbf{x} + \int_{\partial\Omega} \mathbf{t}(t) \cdot \boldsymbol{\Psi}_i \, d\mathbf{s}, \qquad i = 1,...,N_h.$$

Notice that the choice of the basis functions $\{\boldsymbol{\Psi}_i\}$ for the spectral element space $\mathbf{V}_{DG}$ reflects on the structure of system (7). In the following we consider tensor product nodal Lagrangian functions associated with the Gauss-Legendre-Lobatto (GLL) interpolating points for hexahedral elements [20]. This in turn gives a diagonal structure to the matrices M and C that can be effectively exploited for the time integration scheme. Indeed, to integrate (7) in time we proceed as follows. We subdivide the time interval $(0,T]$ into N_T time slabs of length $\Delta t = T/N_T$ and we denote by U^k the approximation of U at time $t^k = k\Delta t$, i.e. $\mathsf{U}^k \approx \mathsf{U}(t_k)$, $k = 0,...,N_T$. Given $\mathsf{U}^0 = \mathsf{U}(0)$ and $\mathsf{V}^0 = \dot{\mathsf{U}}(0)$, to solve system (7) we use the leap-frog scheme:

$$\begin{gathered}
\left(\mathsf{M} + \frac{\Delta t}{2}\mathsf{C}\right)\mathsf{U}^{n+1} = \left(2\mathsf{M} - \Delta t^2\mathsf{A}\right)\mathsf{U}^n - \left(\mathsf{M} - \frac{\Delta t}{2}\mathsf{C}\right)\mathsf{U}^{n-1} + \Delta t^2\mathsf{F}^n,\\
n = 1,\ldots,N_T - 1,
\end{gathered} \tag{8}$$

with initial setup

$$\mathsf{M}\mathsf{U}^1 = \left(\mathsf{M} - \frac{\Delta t^2}{2}\mathsf{A}\right)\mathsf{U}^0 + \left(\Delta t\mathsf{M} - \frac{\Delta t^2}{2}\mathsf{C}\right)\mathsf{V}^0 + \frac{\Delta t^2}{2}\mathsf{F}^0.$$

By taking advantage of the structure of M and C we can easily invert the system $\mathsf{M} + \frac{\Delta t}{2}\mathsf{C}$ in (8). We recall that scheme (8) is explicit and second order accurate, therefore to ensure the numerical stability the Courant-Friedrichs-Lewy (CFL) condition has to be satisfied, see e.g., [65, 21].

We remark that the algorithm presented above can be straightforwardly generalized to the case of a simple nonlinear viscoelastic soil model as the one presented in [28, 80]. The latter is a 3D generalization of the classical $\mu - \gamma$ and $\xi - \gamma$ curves used within

1D linear-equivalent approaches, see, e.g., [50], where γ is the 1D shear strain. In practice, at the generic position $\mathbf{x}$ and generic instant of time t a scalar measure of shear strain amplitude γ is computed, then this value is introduced in the $\mu - \gamma$ and $\xi - \gamma$ curves, and finally the corresponding parameters are updated for the following timestep. Therefore, unlike the classical linear-equivalent approach, the initial values of the dynamic soil properties are recovered at the end of the excitation. The $\mu - \gamma$ and $\xi - \gamma$ curves used for the shallow soil materials are reported in Figure 4.

4 Fragility functions model

The fragility function is a key component of the chain for seismic risk assessment, as it measures the probability of exceeding certain performance (or design) criteria as a function of the level of seismic input intensity, see Equation (1). In general, the fragility function is defined as the conditional probability of a given damage state (or measure) DS exceeding a threshold d_s, given a value of the ground motion intensity measure IM, i.e.

$$\mathrm{FC}(IM, d_s) = P(DS \geq d_s | IM),$$

where $P(A|B)$ is the conditional probability of A given B, cf. [54, 74].

The most common form of a seismic fragility function is the log-normal cumulative distribution function [73, 32], given by

$$\mathrm{FC}(IM, d_s) = \phi\left(\frac{1}{\sigma_s} \ln \frac{IM}{\mu_s}\right), \tag{9}$$

where ϕ is the standard Gaussian cumulative distribution function, μ_s is the median value of the distribution and σ_s is its logarithmic standard deviation for each damage state d_s, $s = 1, \ldots, N$. The log-normal distribution is typically used because: (i) it fits a variety of structural component failure data, as well as non-structural failure data and building collapse by Incremental Dynamic Analyses performed on numerical structural models, see [64]; (ii) it has a strong theoretical basis, being positive definite and fully defined by measures of the first and second statistical moments. The parameters μ_s and σ_s can be evaluated with the use of the maximum likelihood estimation [73, 72, 91, 54] or with the linear regression method [38, 46, 16, 54].

The IM, generically represented in Equations (4) and (9), should be selected according to sufficiency and efficiency criteria depending on the structural typology and on earthquake ground motions (e.g. “ordinary” vs near-source), see [52]. An efficient IM is defined as the one that accurately predicts the response of a structure subjected to earthquake ground motion (i.e. small dispersion of structural response parameters for a given IM), while a sufficient IM is defined as the one that renders structural responses conditionally independent of the earthquake scenario (magnitude and distance). Typical selections for IM are the Peak Ground Acceleration (PGA), the Spectral Acceleration (SA), the Spectral Displacement (SD), or an integral measure of ground shaking, such as the Housner intensity (HI).

As an illustrative example, in Figure 2, we show the family of fragility functions for high-rise buildings (height below 200 m and low seismic design code) developed

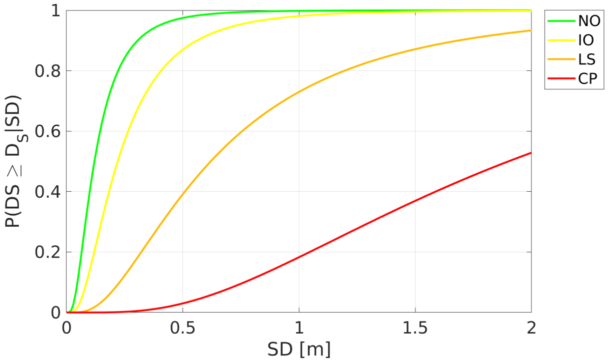

Figure 2: Fragility functions for high-rise buildings – height below 200 meters and low seismic code – according to Wu et al. (2013), where SD is the spectral displacement.

s	d_s	$\mu_s\ (m)$	σ_s
1	NO	0.12	0.73
2	IO	0.22	0.73
3	LS	0.62	0.78
4	CP	1.90	0.71

Table 1: Median Spectral Displacement, μ_s (in meters), and logarithmic standard deviation, σ_s, as retrieved from the fragility functions proposed by Wu et al. (2013) for high-rise buildings with height below 200 meters and low seismic code.

by Wu et al. [84] as a function of spectral displacement SD. Functions are given for the following damage states: Normal Operation (d_1 = NO), Immediate Occupancy (d_2 = IO), Life Safe (d_3 = LS), Collapse Prevention (d_4 = CP). Each function is represented by a log-normal probability distribution, see Equation (9), therefore it is fully described, for each damage state d_s, by the pair (μ_s, σ_s) reported in Table 1.

As summarized by Calvi et al. [19], fragility functions can be obtained by different methods that differ according to the data sources used for their derivation [70, 69, 64]. Empirical approaches require damage data collected during past earthquakes or obtained via experimental tests: the fragility function is then obtained by fitting a function to the observational dataset. Analytical techniques are based on the construction and analysis of a mechanical model of the behavior of the structure subject to seismic shaking. Judgment-based methods rely on the information provided by a team of experts for the asset class in question, who guess or judge the damage probability as a function of seismic excitation. Hybrid fragility functions can be also derived by combining the three approaches above.

A variety of fragility functions has been proposed to assess the seismic vulnerability of structures, such as masonry or reinforced concrete buildings, bridges, shallow tunnels, nuclear plants, wind turbine towers and wharfs, cf. amongst others [23, 13, 66, 17, 73, 72, 82, 16, 71].

5 Earthquake ground motion prediction in the metropolitan area of Beijing

The case study we selected to illustrate the workflow described in Section 2 is the large metropolitan area of Beijing. The population of the Chinese capital grew at a breakneck speed, proving the tendency pointed out by He et al. [43]: the number of inhabitants in China's earthquake-prone areas has increased by over 32 million along with the rapid urbanization. Beijing is situated on a large sedimentary basin and, with its more than 20 million inhabitants and strong urbanization, is one of the many megacities around the world highly exposed to the seismic threat. From an historical point of view Beijing was severely affected by seismic events [41], such as the Sanhe-Pinggu earthquake in 1679, with an estimated magnitude 8, which caused a Modified Mercally intensity of around VIII. In this work, we are interested in investigating the potential rupture of two relevant, well-known seismogenic structures, namely, the Shunyi-Qianmen-Liangxiang and the Nanyuan-Tongxian faults, crossing the metropolitan area of Beijing. Being capable to generate earthquakes up to magnitude 7.3, these faults represent, in fact, a significant threat to the city.

The proximity to these faults along with the complex geological configuration makes the large urban area of Beijing an interesting case study, where non-standard approaches are needed for a more accurate characterization of strong ground motion. To this end, a 3D physics-based numerical model of the Beijing metropolitan area was constructed to simulate a rather large set of earthquake scenarios originating along these faults with magnitude varying from 6.5 to 7.3. Then, seismic risk estimates were obtained by coupling these earthquake ground shaking scenarios with fragility functions for high-rise buildings, the latter ones being an important component of the entire building stock of the city.

Even if some studies adopted physics-based numerical simulation [29] or tried to explicitly model in full 3D the detailed shape of the alluvial basin of Beijing [37], to our knowledge, none of the previous investigations have considered a large number of earthquake scenarios occurring along the two aforementioned faults. Furthermore, in those studies, no attempt was made to use synthetic ground motion scenarios to generate seismic damage scenarios for specific building typologies existing in this hazardous area.

The intent of this work is not to provide a comprehensive seismic hazard/risk analyses of the Beijing area, as it has already been performed previously by other authors [85, 86], rather to provide insights into the potential advantages of using PBS to provide site-specific evaluations of the earthquake ground motion in complex near-field geological conditions. Furthermore, as already pointed out by Xiong et al. [88], our synthetic seismograms obtained via wave propagation simulation might be used as input for dynamic response history analyses of buildings requiring the entire time history rather than IM values, as recently done by Xu et al. and Lu et al. [90, 51].

Segment	L_{max} $[km]$	W_{max} $[km]$	Strike $(^\circ)$	Dip $(^\circ)$	Top Depth $[m]$	Fault Origin $(Lat\,[^\circ N],\, Lon[^\circ E])$
North	24.9	30	44	80	38.8	(40.02, 116.52)
Middle	29.7	30	48	80	51.9	(39.84, 116.27)
South	35.6	30	30	80	31.7	(39.56, 116.07)

Table 2: Geometric parameters of the Shunyi-Qianmen-Liangxiang fault. Fault origin indicates the vertex of the fault at zero strike and dip.

5.1 Set-up of the 3D numerical model

The 3D computational domain for the Beijing area was set up considering the following input models and data: (i) the topography model, (ii) the seismic fault whose rupture is modelled using a kinematic representation, (iii) the 3D subsoil structure accounting for the variable thickness of the sedimentary basin and the 3D velocity profiles, cf. [8]. The topography model was built from freely-available digital elevation dataset of CGIAR-CSI for the Beijing area (downloaded from the website `http://srtm.csi.cgiar.org`). The data have a resolution of approximately 90×90 m, for north-south and east-west directions.

Among the relevant seismic sources (i.e. Shunyi-Qianmen-Liangxian, SQL, and Nanyuan-Tongxian, NT, faults), for sake of presentation, herein we investigate earthquake rupture scenarios occurring only along the SQL fault system which crosses the central Beijing area. It is a normal quasi-vertical (the dip angle is about 80°) fault consisting of three main segments with different strike angles. The total fault length is about 90 km and it can produce events up to M_w 7.3. In Table 2 we report the geometric parameters of the SQL fault, as implemented in our computational model.

As regards the 3D soil model, it was constructed by merging data regarding both the geologic structure of the alluvial basin, see Figure 3 (top left), and the spatial distribution of $V_{s,30}$ (weighted average shear wave velocity in the top 30 m), cf. Figure 3 (top right) and [3]. The former was derived from the digitalization of the model proposed in [37], while the latter was adapted from `https://earthquake.usgs.gov/data/vs30`. In particular, given z_{top} and z_{sed}, that represent the projection of a generic point with coordinate z into the surface and the sediment base, respectively, we have considered for the first layer (0 to 2 km depth) the following properties, cf. Figure 3 (bottom),

$$\begin{cases} v_s = & V_{s,30} + 5\sqrt{|z - z_{top}|},\ v_p = 1.6 v_s, \\ & \qquad \text{for } V_{s,30} \geq 600\, m/s, \\ v_s = & V_{s,30} + 10\sqrt{|z - z_{top}|},\ v_p = 1.6 v_s, \\ & \qquad \text{for } V_{s,30} < 600\, m/s,\ z \geq z_{sed}, \\ v_s = & 800 + 10\sqrt{|z - z_{top}|},\ v_p = 2000 + 15\sqrt{|z - z_{top}|}, \\ & \qquad \text{for } V_{s,30} < 600\, m/s,\ z < z_{sed}, \end{cases} \tag{10}$$

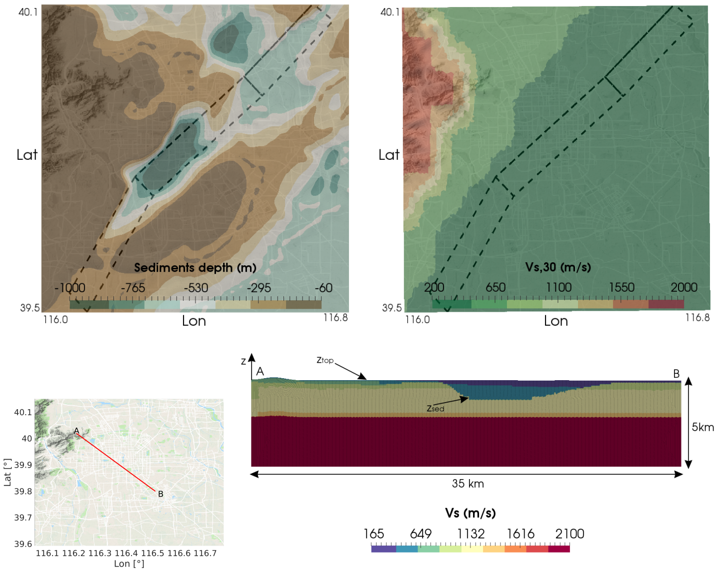

Figure 3: Sediment thickness (top left) and $V_{s,30}$ model (top right). Black rectangles represent the surface projection of the considered Shunyi-Qianmen-Liangxiang (SQL) fault. Bottom: geologic cross-section $A - B$ (see map on the left) showing the distribution of $v_s(z)$ for the first layer 0-2 km (right).

where the different velocity profiles are in m/s. Similarly, we defined the soil density in kg/m^3 as follows

$$\begin{cases} \rho = 1800 + 5\sqrt{|z - z_{top}|}, & \text{for } V_{s,30} \geq 600\, m/s, \\ \rho = 1530 + 5\sqrt{|z - z_{top}|}, & \text{for } V_{s,30} < 600\, m/s,\ z \geq z_{sed}, \\ \rho = 1800 + 5\sqrt{|z - z_{top}|}, & \text{for } V_{s,30} < 600\, m/s,\ z < z_{sed}. \end{cases} \tag{11}$$

In addition, we consider a non-linear soil behaviour of the soft soil deposits ($V_{s,30} \leq 400\ m/s$ and $z_{top} \leq z \leq z_{top} - 300\ m$), as described in Section 3, based on the modulus reduction and damping curves shown in Figure 4.

Dynamic properties for the underlying bedrock layers (depth $> 2\ km$), assumed to be horizontally stratified, have been assigned in accordance with [37], see Table 3. The computational domain was built by considering all the information above and extends over an area of $70 \times 70\ km^2$ down to 30 km depth (see Figure 5). In order to correctly simulate in SPEED the earthquake ground motion up to a maximum frequency $f = 1.5\ Hz$, we built a conforming mesh with size of 150 m on the top surface, of 600 m at 4 km depth and reaching 1800 m in the underlying layers. In particular the model consists of 859.677 hexahedral elements and, by using a fourth order polynomial approximation degree $p = 4$, it has approximately 160 million degrees of freedom.

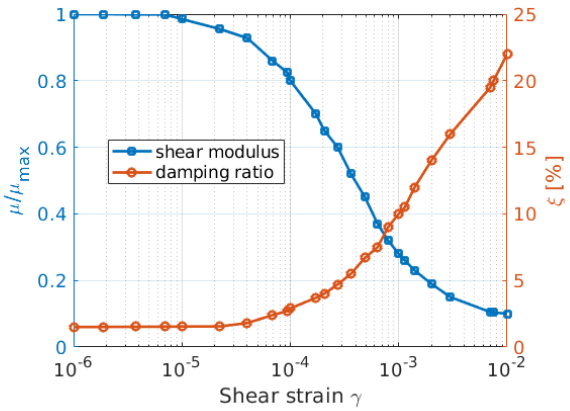

Figure 4: Curves of normalized shear modulus μ and damping ratio ξ as a function of shear strain γ, adopted for the alluvium shallow materials in the Beijing basin.

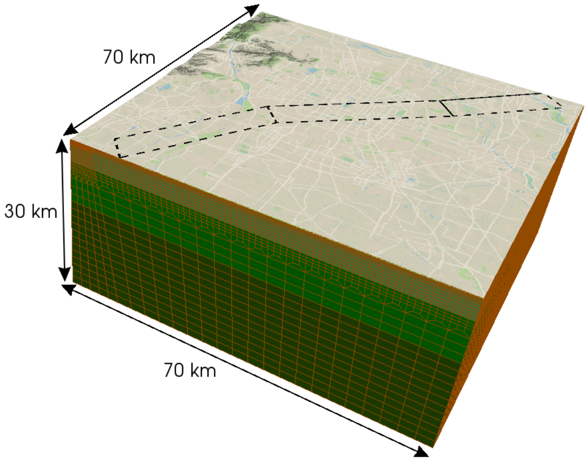

Figure 5: 3D computational model for the Beijing area with indication of the SQL fault.

Layer	Depth $[km]$	$v_s\,[m/s]$	$v_p\,[m/s]$	$\rho\,[km/m^3]$	$\xi\,[mHz]$
1	0 – 2		see (10) – (11)		$15\pi/v_s$
2	2 – 4	2100	3500	2200	22.44
3	4 – 12	3400	6000	2760	13.86
4	12 – 30	3500	6200	2810	13.46

Table 3: Horizontally stratified crustal model, from Gao et al. (2014).

Scenario: M_w	Simulated footprints	Rupture area ($km \times km$)
6.5	15	24×12
6.9	10	36×18
7.3	5	54×24

Table 4: Summary of PBS for the Beijing case study. Simulated footprints for each earthquake scenario with given M_w.

Then we fixed the total observation time $T = 60$ s and we used a time step $\Delta t = 0.001$ s. The walltime for each simulation is around 12 hours on 512 cores on the Marconi cluster at CINECA, Italy (`http://www.cineca.it/en/content/marconi`).

To capture the variability of earthquake ground motion resulting from different fault ruptures along the SQL fault, a set of 30 PBSs (footprints according to the terminology previously introduced) was performed by varying the moment magnitude M_w, from a minimum of 6.5 up to a maximum of 7.3, the location of the hypocenter, the kinematic slip distribution on the fault and the rupture area location. A summary of the simulated seismic footprints, grouped according to the three magnitude levels (i.e. scenario), is provided in Table 4.

The main kinematic parameters of the slip distributions for a given fault and a given earthquake magnitude were chosen by considering probability distributions ensuring that the resulting scenario variability is not affected by systematic bias in the input parameters. For each scenario we employed the kinematic source rupture generator proposed by Crempien and Archuleta [25]. As an example, Figure 6 shows the fault rupture realizations considered for four selected footprints, namely 4/15 and 6/15 for scenario M_w 6.5, 8/10 for scenario M_w 6.9 and 1/5 for scenario M_w 7.3, which will considered in further details in the following.

5.2 Discussion of results of 3D PBS

In the following, some representative results of the 3D physics-based numerical simulations will be discussed with emphasis on the characterization of earthquake ground motion. Figure 7 shows some snapshots of the velocity wave field (modulus of horizontal components) for the footprint 4/15 – scenario M_w 6.5. Interestingly, two large pulses, pointing south-west and north-east with respect to the epicenter and almost aligned along the surface projection of the top segment of the fault, are clearly visible. These pulses are associated with rupture directivity effects (see also Figure 6) as can be observed also in the velocity time histories, EW component, illustrated in Figure 8 for

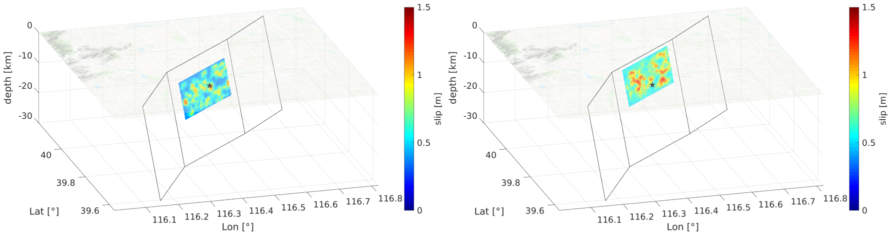

(a) Footprint 4/15 – Scenario M_w 6.5 (b) Footprint 6/15 – Scenario M_w 6.5

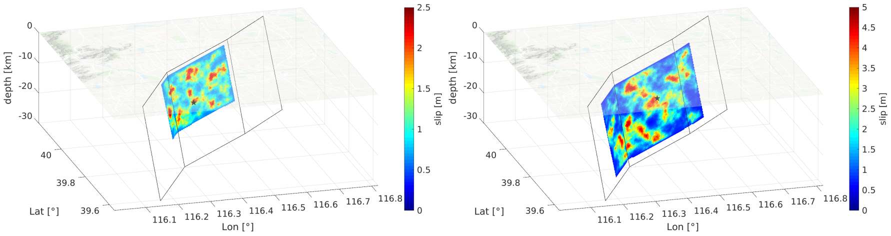

(c) Footprint 8/10 – Scenario M_w 6.9 (d) Footprint 1/5 – Scenario M_w 7.3

Figure 6: Distribution of the slip pattern along the fault and hypocenter location (black star) for four selected footprints corresponding to earthquake scenarios with M_w 6.5, 6.9 and 7.3.

7 representative sites, more specifically at stations 2, 3 and 4, lying above the surface projection of the fault.

As already proposed by Villani et al. [81], for each Scenario the first statistical moments obtained for the relevant ground motion parameters from the population of synthetic signals (at the sites of interest) can be computed, and used in the same way as one would use the median and the sigma of a classical GMPE. Figure 9 (left column) shows the map of the median values (first statistical moment) of the peak ground velocity (PGV, geometric mean of horizontal components), computed from all set of simulated footprints for each scenario magnitude: M_w 6.5 (top), M_w 6.9 (middle) and M_w 7.3 (bottom), cf. Table 4. The right column of Figure 9 compares the median PGV, obtained by means of the physics-based approach (SPEED simulations) against the one based on the GMPE proposed by Cauzzi et al. [22], referred to as CAEA15 hereafter. For simplicity, the GMPE was calculated assuming an average $V_{s,30}$ equal to 235 m/s, being this value relatively constant throughout the whole metropolitan area of Beijing. Consistently to the chosen GMPE, the metric adopted for the comparison is the closest distance to the fault rupture (R_{rupt}). Note that, for scenario $M_w 7.3$, the minimum rupture distances are larger than the ones for other scenarios, because of the larger depth of the rupture area (see Figure 6).

It is worth to highlight that the PBS obtained by SPEED present an overall good agreement with the prediction of the GMPE. However, PBS produce median peak ground values systematically higher at short distances from the fault (typically for R_{rupt} less than around 5 km) and generally lower at longer distances. Furthermore, the standard deviation computed from our site-specific simulations tends to be smaller than the one

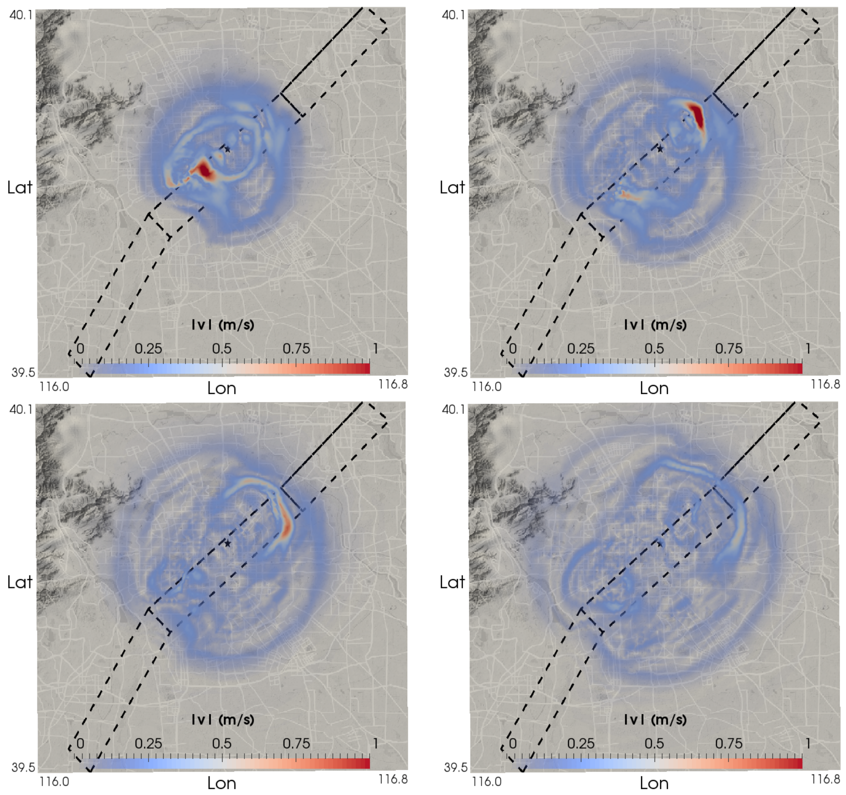

Figure 7: Snapshots of the velocity wave field obtained for footprint 4/15 with M_w 6.5, cf. Table 4. Top-left: $t = 7\ s$, top-right: $t = 8\ s$, bottom-left: $t = 9\ s$, bottom-right: $t = 10\ s$.

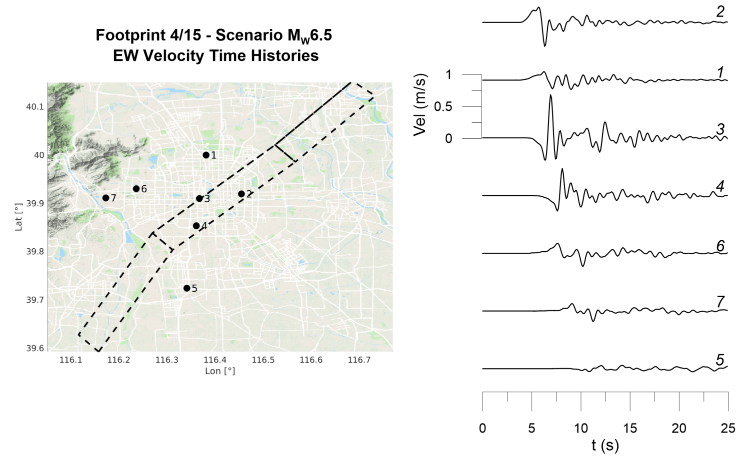

Figure 8: Velocity time histories (low-pass filter at 1.5 Hz), EW component, at 7 representative sites of the model.

from CAEA15, as the latter is increased because of the ergodic assumption, applied to site-generic applications of earthquake ground motion modeling. Since the GMPE may not, or may only partially, consider certain specific effects like the near-field or alluvial basin, cf. [60], comparison of GMPE and PBS results should be generally recommended whenever PBS are carried out and such site-specific effects on seismic wave propagation have to be identified and quantified.

6 Seismic risk assessment for high-rise buildings

The aim of this Section is to apply the workflow presented in Section 2 to generate seismic damage scenarios for the class of high-rise buildings in the urban area of Beijing. As previously mentioned, high-rise buildings represent a significant portion of the building stock in Beijing exposed to seismic risk. Although an exhaustive analysis of the Chinese fragility functions has been proposed by Xin et al. [87], in this work, we focus on a special class of buildings: the so-called super high-rise buildings with height over 100 m, cf. [56, 48]. For this purpose, the results of PBS, introduced in previous Section, are coupled with the fragility functions developed by Wu et al. [84] specifically for Chinese high-rise buildings. For simplicity, results will be only provided in terms of seismic damage assessment, while the extension to comprehensive seismic risk evaluation including fatality and/or loss assessment is beyond the scope of this work.

Starting from the published data regarding more than 50 high-rise buildings, Wu et al. [84] developed regression analyses between the maximum storey drift ratios and the response spectral displacement for high-rise buildings located in China. Fragility functions were then proposed for different categories of high-rise buildings, depending

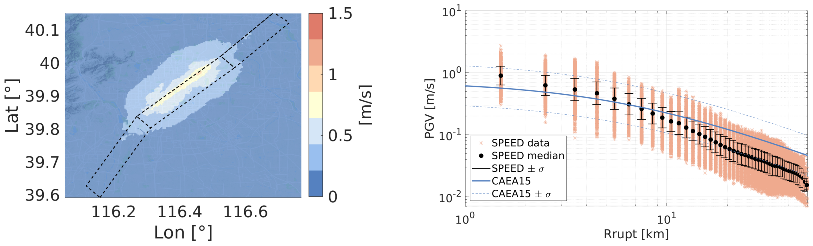

(a) All Scenarios – M_w 6.5 (b) All Scenarios – M_w 6.5

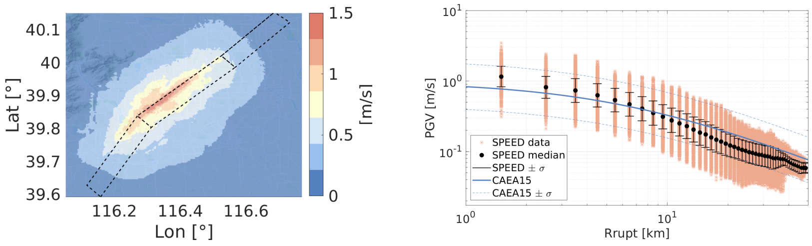

(c) All Scenarios – M_w 6.9 (d) All Scenarios – M_w 6.9

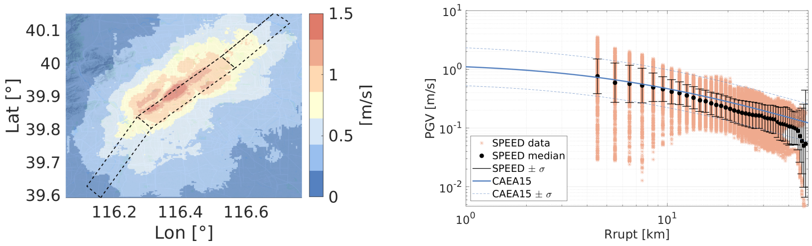

(e) All Scenarios – M_w 7.3 (f) All Scenarios – M_w 7.3

Figure 9: Left column: Median PGV (geometric mean of horizontal components) maps obtained by considering all footprints for scenarios with M_w 6.5 (top), M_w 6.9 (middle) and M_w 7.3 (bottom). Right column: comparison with the GMPE by Cauzzi et al. (2015), (CAEA15) against physics-based scenarios. Pink stars show PGV simulated at each receiver for each individual footprint, while black dots represent the median and the bar the dispersion around that value.

on the building height (above 200 m and below 200 m) and the level of seismic design code (low, moderate and high), and for the following damage states: Normal Operation (NO), Immediate Occupancy (IO), Life Safe (LS), Collapse Prevention (CP). These four classes can be described in terms of damage levels as follows: NO = very light, IO = light, LS = moderate and CP = severe, cf. FEMA273 [24]. In our analysis, without loss of generality, we focus on the category of high-rise buildings with height below 200 m and low prescriptions levels for seismic design, see Figure 2 and Table 1 in Section 4.
Considering buildings with height of approximately 100 m, for which, on average, a fundamental period of vibration of $3s$ can be defined based on statistical analysis of vibration properties of Chinese high-rise buildings [89], spectral displacement (SD) at 3 s was assumed as a ground motion proxy for the fragility functions.

Figure 10 shows the probability of exceeding the LS damage state as a function of R_{rupt}, for the four previously selected footprints corresponding to three scenarios (M_w 6.5, 6.9 and 7.3). Note that these plots show footprints-based estimates, therefore they provide the probability of exceedance of damage state LS, conditioned to the value of IM attained at any site of the model, i.e. $P(DS \geq \text{LS}|IM)$. Pink stars represent $P(DS \geq \text{LS}|IM)$ for all the receivers included in our computational model within a given distance bin, while the black dots and bars show the corresponding mean and $\pm\sigma$ values, respectively. Results obtained from the PBS are compared with those obtained employing the median and $16/84^{th}$ percentiles values of $SD(3s)$ provided by CAEA15. Consistently with the previous comment on ground motion, the probability of LS damage state differs significantly at short distances: PBS estimates provides remarkable higher values compared to the GMPE based one. At around 10 km distance the discrepancy tends to vanish also due to the fact that 3 footprints out of the 4 selected, are clearly showing an almost negligible probability associated to this specific damage state.

In Figure 11 we report the probability of exceeding the different damage states, specifically, white – No Damage (ND), green – Normal Operation (NO), yellow – Immediate Occupancy (IO), orange – Life Safe (LS) and red – Collapse Prevention (CP), as a function of R_{rupt}, for the 4 selected footprints. The plot interestingly shows, on the one hand, a very steep reduction of the mean damage state probabilities and, on the other, an impressively stable trend of the dispersion around the mean value. Particularly because of the latter fact, it is important to consider PBS, aiming at explaining this variability from a physical point of view and to spatially correlate it to the fault rupture. In a nutshell, these preliminary analyses show that in the near-field region a systematic bias between GMPE and PBS can be observed, and that the probability of exceeding two critical damage levels (LS and CP) is very significant.

Given the location of the Shunyi-Qianmen-Liangxiang fault, a rather large portion of the metropolitan area of Beijing falls in this near-field range. In Tables 5 and 6, for the four selected footprints, the probability associated to each performance level is depicted as a pie chart where the different colors denote the damage states, as already described for Figure 11. We observe the following tendency: starting from footprint 4/15 (M_w 6.5) the dominating effects are null and slight damages (colors white and green), while footprint 1/5 (M_w 7.3) shows a predominance of significant and severe damages up to collapse (colors yellow, orange and red). Furthermore, comparing re-

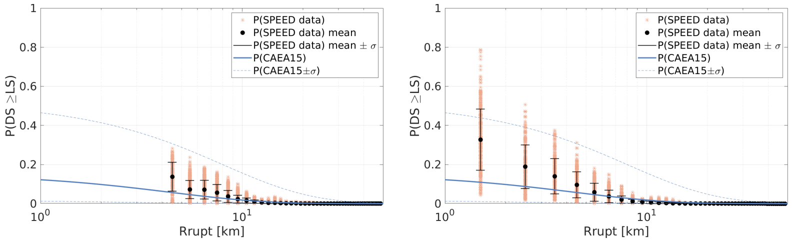

(a) Footprint 4/15 – Scenario M_w 6.5 (b) Footprint 6/15 – Scenario M_w 6.5

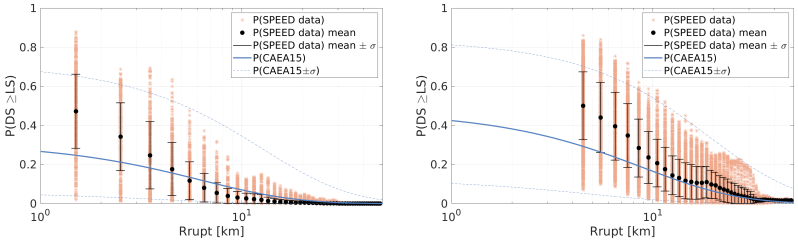

(c) Footprint 8/10 – Scenario M_w 6.9 (d) Footprint 1/5 – Scenario M_w 7.3

Figure 10: Probability of exceeding damage state (DS) greater than or equal to Life Safe (LS) versus the closest distance to the fault rupture (R_{rupt}). Pink stars denote the $P(DS \geq \text{LS}|IM)$ for each simulated receiver within the Beijing area, while filled black dots and bars represent the corresponding mean and standard deviation.

sults obtained for the different sites, it is evident that sites 2, 3 and 4, located on the surface projection of the fault, show, across all Scenario footprints, the most dangerous damage estimates.

So far, seismic risk scenarios were generated for specific earthquake footprints in a deterministic way ($L1$ risk analysis), focusing on the analysis of the damage distribution as a function of the distance from the causative fault. Finally, to shed light on the potential use of 3D PBS within probabilistic frameworks for seismic risk assessment, $P(DS \geq d_s|scenario)$ was computed by the convolution integral of Equation (1) according to the procedure devised in Section 2 ($L2$ risk analysis).

Referring to the earthquake scenario with magnitude $M_w = 6.5$ (illustrated herein), for any site of the model, the probability of different damage states was derived by taking into account all 15 earthquake footprints simulated for this scenario (see Table 4). This means that, under the assumption of a log-normal probability density function for $SD(3s)$ (see Equation (2)), $\mu_{SD(3s)}$ and $\sigma_{SD(3s)}$ are estimated, for the selected scenario magnitude, from the corresponding set of footprints by using the maximum likelihood method. The results for earthquake scenario $M_w = 6.5$ along the SQL fault obtained at the 7 sites under consideration are shown in Table 7 in terms of $\mu_{SD(3s)}$, $\sigma_{\log_{10} SD(3s)}$ and $P(DS = d_s|scenario\ M_w 6.5)$ for the different damage states. For the same scenario earthquake, Figure 12 illustrates the spatial distribution of damage probabilities $P(DS \geq d_s|scenario\ M_w 6.5)$ obtained by means of PBS. Analogously to Table 7 and in order to highlight the differences that may arise adopting GMPEs,

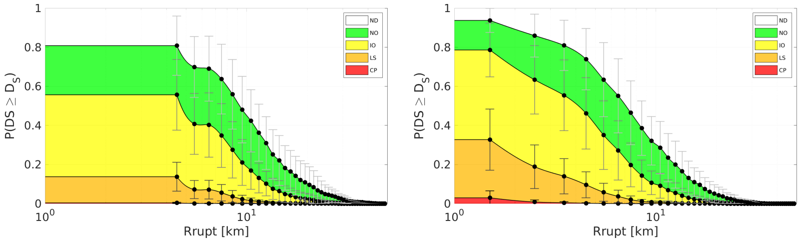

(a) Scenario 5 – M_w 6.5 (b) Scenario 7 – M_w 6.5

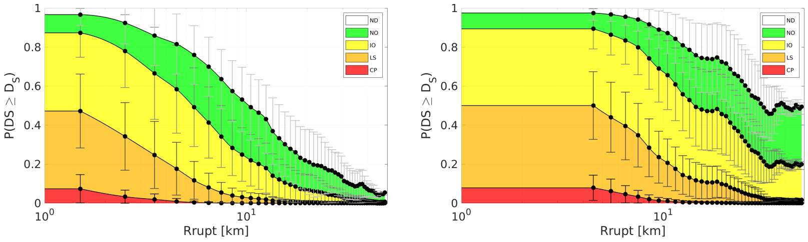

(c) Scenario 21 – M_w 6.9 (d) Scenario 22 – M_w 7.3

Figure 11: Probability of exceeding all Damage States (DS) as a function of R_{rupt}: white – No Damage (ND), green – Normal Operation (NO), yellow – Immediate Occupancy (IO), orange – Life Safe (LS) and red – Collapse Prevention (CP). Filled black dots: mean; bars: standard deviation.

Table 8 shows the results obtained through CAEA15 for the same scenario earthquake. Note that top rows of both Tables 7 and 8 illustrate the map of $\mu_{SD(3s)}$ $\sigma_{\log_{10} SD(3s)}$ from PBS and CAEA15, respectively. From the comparison of these maps, it is clear that: (i) median values from PBS show a steep gradient of the ground motion predicted in the proximity of the fault owing to the coupling of source rupture effects with complex site effects in the Beijing basin; (ii) σ values from PBS tend to be smaller, on average, than the ones from CAEA15 as the former are site-specific (i.e. ergodic assumption is removed, see [2]); furthermore, PBS produce dispersion values characterised by a strong spatial dependency, which cannot, or can only partially, be accounted for in GMPEs.

7 Conclusions

In this work we have introduced a novel approach for seismic risk assessment which couples 3D physics-based scenarios (PBSs) and standard fragility functions in order to obtain an alternative and complementary risk estimate to the more classical one, based on Ground Motion Prediction Equations (GMPEs). As it is well known, scenarios generated by empirical GMPEs present some major benefits as proven by the fact that they have been used for decades. Despite that, it is also worth to underline that, especially in the near-field of an earthquake, the number of records might be not sufficient to satisfactorily constrain the expected site-specific ground motion spatial

- ⬜ ND
- 🟩 NO
- 🟨 IO
- 🟧 LS
- 🟥 CP

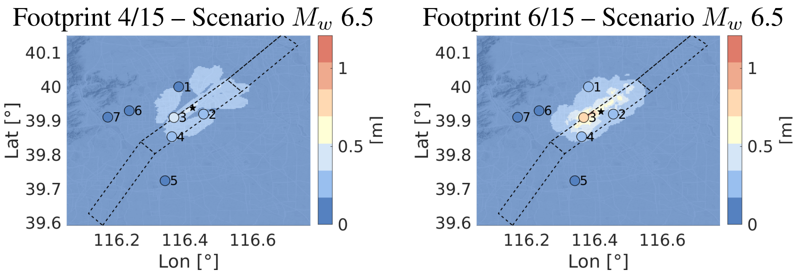

Location ID	R_{rupt} $[km]$	PGV $[m/s]$	$SD(3s)$ $[m]$	DS $[\%]$	R_{rupt} $[km]$	PGV $[m/s]$	$SD(3s)$ $[m]$	DS $[\%]$
1	9	0.23	0.15	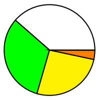	7	0.31	0.22	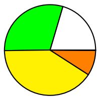
2	6	0.39	0.18	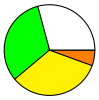	4	0.47	0.29	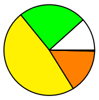
3	5	0.81	0.35	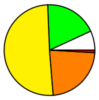	1	2.10	0.81	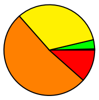
4	6	0.47	0.21	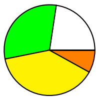	4	0.55	0.28	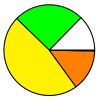
5	16	0.09	0.10	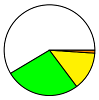	16	0.10	0.07	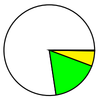
6	11	0.16	0.07	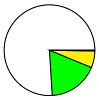	10	0.16	0.09	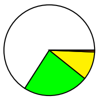
7	14	0.10	0.04	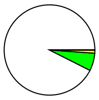	13	0.10	0.05	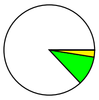

Table 5: Summary table providing damage predictions for selected earthquake footprints and selected locations in the Beijing area. For each footprint (ordered on the columns, 4/15 – M_w 6.5 and 6/15 – M_w 6.5) and each location (ordered on the rows, from 1 to 7) we report: 1) maps in terms of SD at $T = 3\ s$; 2) values of PGV and $SD(3s)$ and 3) pie charts showing $P(DS = d_s)$, with colors denoting the different damage states (white: no damages – ND; green: very light damages, normal operation – NO; yellow: light damages, immediate occupancy – IO; orange: moderate damages, life safe – LS; red: severe damages, collapse prevention – CP).

⬜ ND
🟩 NO
🟨 IO
🟧 LS
🟥 CP

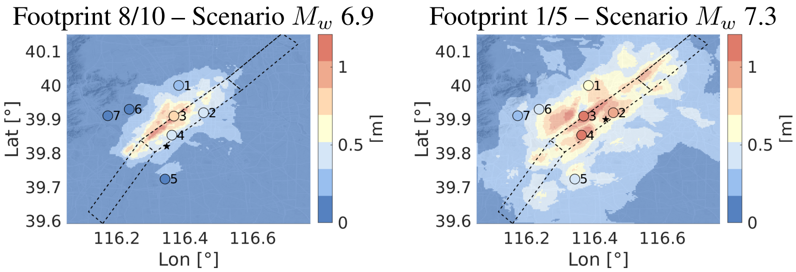
Footprint 8/10 – Scenario M_w 6.9

Footprint 1/5 – Scenario M_w 7.3

Location ID	R_{rupt} $[km]$	PGV $[m/s]$	$SD(3s)$ $[m]$	DS $[\%]$	R_{rupt} $[km]$	PGV $[m/s]$	$SD(3s)$ $[m]$	DS $[\%]$
1	7	0.39	0.25	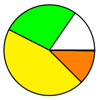	8	1.32	0.67	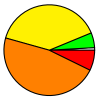
2	4	0.68	0.41	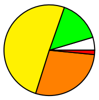	5	1.86	1.04	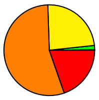
3	1	1.75	0.84	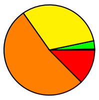	4	3.10	1.26	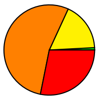
4	4	0.67	0.49	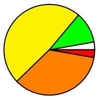	5	1.38	1.04	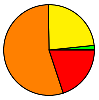
5	11	0.20	0.16	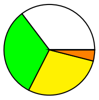	12	0.55	0.51	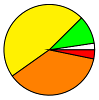
6	10	0.25	0.10	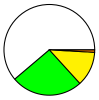	11	0.78	0.43	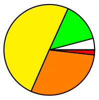
7	12	0.18	0.08	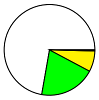	13	0.56	0.28	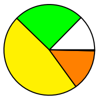

Table 6: As in Table 5 but with footprints (ordered on the columns) 8/10 – M_w 6.9 and 1/5 – M_w 7.3.

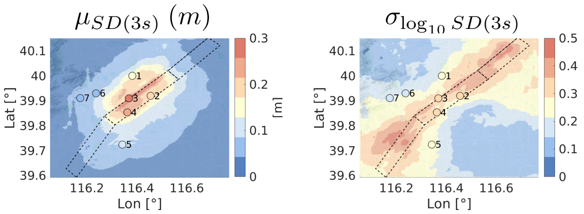

ID	1	2	3	4
$\mu_{SD(3s)}\ (m)$	0.16	0.19	0.29	0.24
$\sigma_{\log_{10} SD(3s)}$	0.22	0.31	0.31	0.30
DS	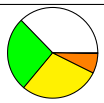	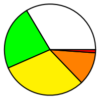	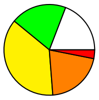	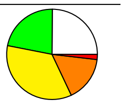

ID	5	6	7
$\mu_{SD(3s)}\ (m)$	0.09	0.08	0.05
$\sigma_{\log_{10} SD(3s)}$	0.24	0.19	0.21
DS	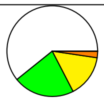	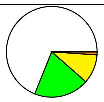	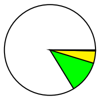

Table 7: Summary table providing damage predictions for selected locations in Beijing area, considering all SPEED footprints for earthquake scenarios with M_w 6.5. For each location (ordered on the columns, from 1 to 7), the first statistical moments of $SD(3s)$, i.e. $(\mu_{SD(3s)}, \sigma_{\log_{10} SD(3s)})$, along with the pie charts of damage probabilities, are shown. Colors for damage states are the same as used in previous graphs.

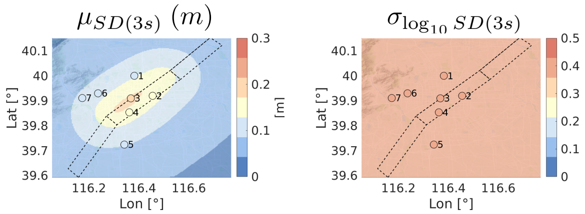

ID	1	2	3	4
$\mu_{SD(3s)}$ (m)	0.12	0.15	0.18	0.16
$\sigma_{\log_{10} SD(3s)}$	0.36	0.36	0.36	0.36
DS	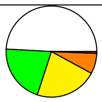	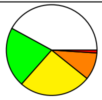	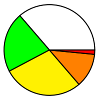	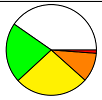

ID	5	6	7
$\mu_{SD(3s)}$ (m)	0.09	0.11	0.10
$\sigma_{\log_{10} SD(3s)}$	0.36	0.36	0.36
DS	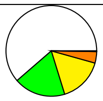	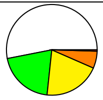	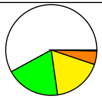

Table 8: As in Table 7 but using median and standard deviation values from the GMPE of CAEA15.

distribution, including peculiar effects, such as directivity or spatial correlation of the ground motion. For this reason, instead of GMPEs, we simulated PBSs by solving the wave propagation problem with the SPEED code that is based on the Discontinuous Galerkin Spectral Element Method. Once a relatively large set of synthetic scenarios was generated, we combined the synthetic ground motions with classical fragility functions in order to finally evaluate the seismic risk for any specific class of buildings. As a case study of the above mentioned workflow, the large metropolitan area of Beijing was considered, the seismic hazard of which is governed by the Shunyi-Qianmen-Liangxiang and Nanyuan-Tongxian faults. For this purpose, a set of PBSs was obtained with magnitudes ranging from a minimum of 6.5 up to a maximum of 7.3; the location of hypocenter, the slip patterns and other parameters have been systematically varied, aiming at covering, as much as possible, the variability of seismic shaking, associated with the different ruptures that might realistically take place in the future. The potential consequences of such scenarios have been investigated, focusing on the structural response of the high-rise building class, particularly relevant in Beijing. To this end, we adopted fragility functions explicitly calibrated for the Chinese building stock.

Our analyses suggest that PBSs can be fruitfully adopted for seismic risk assessment purposes. The comparison against GMPEs revealed that systematic differences take place especially in the near-field region. Considering the fact that GMPEs tend to lack of calibration data in this area and that PBSs are intrinsically physically con-

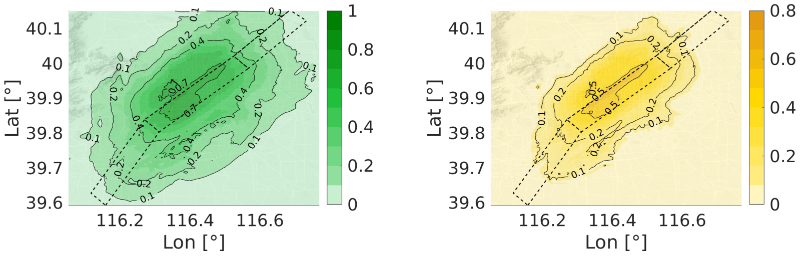

(a) $P(DS \geq \text{NO})$ (b) $P(DS \geq \text{IO})$

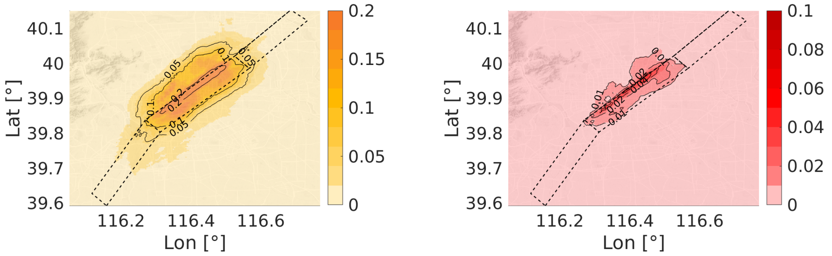

(c) $P(DS \geq \text{LS})$ (d) $P(DS \geq \text{CP})$

Figure 12: Seismic damage maps for high-rise buildings, in terms of $P(DS \geq d_s | scenario\ M_w = 6.5)$, accounting for all footprints corresponding to a scenario earthquake with M_w 6.5.

strained, we conclude that the PBS methodology may be complementary to GMPEs, in all cases where the seismogenic structure that govern local seismic hazard are known and a sufficiently accurate 3D model of the local geology may be constructed.

Acknowledgments

P. F. Antonietti, I. Mazzieri and L. Melas have been partially supported by SIR (Scientific Independence of young Researchers) starting grant n. RBSI14VT0S funded by the Italian Ministry of Education, Universities and Research (MIUR). This work was also partially supported by Munich RE.
We acknowledge the CINECA HPC supporting under the ISCRA initiative for the availability of high performance computing resources and support. The authors would like also to thank Maria Infantino for her valuable help with post-processing analysis of 3D physics-based scenarios.

References

[1] K. Aki and P. G. Richards. *Quantitive Seismology: Theory and Methods*, volume 1. Freeman, San Francisco, California, 2002.

[2] L. Al Atik, N. Abrahamson, J. Bommer, F. Scherbaum, F. Cotton, and N. Kuehn. The variability of ground-motion prediction models and its components. *Seismological Research Letters*, 81(5):794–801, 2010.

[3] T. I. Allen and D. J. Wald. On the use of high-resolution topographic data as a proxy for seismic site conditions (VS30). *B. Seismol. Soc. Am.*, 99(2A):935–943, 2009.

[4] P. Antonietti, F. Bonaldi, and I. Mazzieri. A high-order discontinuous Galerkin approach to the elasto-acoustic problem. *MOX report, 18/2018*, 2018.

[5] P. Antonietti, F. Bonaldi, and I. Mazzieri. Simulation of 3D elasto-acoustic wave propagation based on a discontinuous Galerkin spectral element method. *MOX report, 26/2019*, 2019.

[6] P. Antonietti, N. Dal Santo, I. Mazzieri, and A. Quarteroni. A high-order discontinuous Galerkin approximation to ordinary differential equations with applications to elastodynamics. *IMA J. Numer. Anal.*, 38(4):1709–1734, 2018.

[7] P. F. Antonietti, B. Ayuso de Dios, I. Mazzieri, and A. Quarteroni. Stability analysis of discontinuous Galerkin approximations to the elastodynamics problem. *J. Sci. Comput.*, 68(1):143–170, 2016.

[8] P. F. Antonietti, A. Ferroni, I. Mazzieri, R. Paolucci, A. Quarteroni, C. Smerzini, and M. Stupazzini. Numerical modeling of seismic waves by discontinuous spectral element methods. *ESAIM: Proceedings and Surveys*, 61:1–37, 2018.

[9] P. F. Antonietti, A. Ferroni, I. Mazzieri, and A. Quarteroni. hp-version discontinuous Galerkin approximations of the elastodynamics equation. In *Spectral and high order methods for partial differential equations—ICOSAHOM 2016*, volume 119 of *Lect. Notes Comput. Sci. Eng.*, pages 3–19. Springer, Cham, 2017.

[10] P. F. Antonietti and I. Mazzieri. High-order Discontinuous Galerkin methods for the elastodynamics equation on polygonal and polyhedral meshes. *Comput. Methods Appl. Mech. Engrg.*, 342:414–437, 2018.

[11] P. F. Antonietti, I. Mazzieri, and A. Quarteroni. Improving seismic risk protection through mathematical modeling. In *Imaging Maths. Between culture and mathematics: 4*, pages 271–282. M. Emmer, M. Abate, M. Villarreal Editors, 2015.

[12] P. F. Antonietti, I. Mazzieri, A. Quarteroni, and F. Rapetti. Non-conforming high order approximations of the elastodynamics equation. *Comput. Methods Appl. Mech. Engrg.*, 209/212:212–238, 2012.

[13] S. Argyroudis and K. Pitilakis. Seismic fragility curves of shallow tunnels in alluvial deposits. *Soil Dyn. Earthq. Eng.*, 35:1–12, 2012.

[14] D. N. Arnold. An interior penalty finite element method with discontinuous elements. *SIAM J. Numer. Anal.*, 19(4):742–760, 1982.

[15] D. N. Arnold, F. Brezzi, B. Cockburn, and L. D. Marini. Unified analysis of discontinuous Galerkin methods for elliptic problems. *SIAM J. Numer. Anal.*, 39(5):1749–1779, 2001/02.

[16] S. Banerjee and M. Shinozuka. Mechanistic quantification of RC bridge damage states under earthquake through fragility analysis. *Probabilist. Eng. Mech.*, 23(1):12–22, 2008.

[17] E. Borgonovo, I. Zentner, A. Pellegri, S. Tarantola, and E. de Rocquigny. On the importance of uncertain factors in seismic fragility assessment. *Reliab. Eng. Syst. Safe.*, 109:66–76, 2013.

[18] B. Bradley. On-going challenges in physics-based ground motion prediction and insights from the 2010–2011 Canterbury and 2016 Kaikoura, New Zealand earthquakes. *Soil Dyn. Earthq. Eng.*, 2018.

[19] G. M. Calvi, R. Pinho, G. Magenes, J. J. Bommer, L. F. Restrepo-Vélez, and H. Crowley. Development of seismic vulnerability assessment methodologies over the past 30 years. *ISET Journal of Earthquake Technology*, 43(3):75–104, 2006.

[20] C. Canuto, M. Y. Hussaini, A. Quarteroni, and T. A. Zang. *Spectral methods – Fundamentals in single domains*. Scientific Computation. Springer-Verlag, Berlin, 2006.

[21] C. Canuto, M. Y. Hussaini, A. Quarteroni, and T. A. Zang. *Spectral methods – Evolution to complex geometries and applications to fluid dynamics*. Scientific Computation. Springer, Berlin, 2007.

[22] C. Cauzzi, E. Faccioli, M. Vanini, and A. Bianchini. Updated predictive equations for broadband (0.01–10 s) horizontal response spectra and peak ground motions, based on a global dataset of digital acceleration records. *B. Earthq. Eng.*, 13(6):1587–1612, 2015.

[23] J.-S. Chiou, C.-H. Chiang, H.-H. Yang, and S.-Y. Hsu. Developing fragility curves for a pile-supported wharf. *Soil Dyn. Earthq. Eng.*, 31(5-6):830–840, 2011.

[24] B. S. S. Council. NEHRP guidelines for the seismic rehabilitation of buildings. *FEMA-273, Federal Emergency Management Agency, Washington, DC*, 1997.

[25] J. G. Crempien and R. J. Archuleta. UCSB method for simulation of broadband ground motion from kinematic earthquake sources. *Seismol. Res. Lett.*, 86(1):61–67, 2015.

[26] S. Detweiler and A. Wein. The HayWired earthquake scenario–Earthquake hazards. *Scientific Investigations Report*, 2017–5013(A–H), 2017. 126 p., U.S Geological Survey.

[27] S. Detweiler and A. Wein. The HayWired earthquake scenario–Engineering implications. *Scientific Investigations Report*, 2017–5013(I–Q), 2018. 429 p., U.S Geological Survey.

[28] C. di Prisco, M. Stupazzini, and C. Zambelli. Nonlinear SEM numerical analyses of dry dense sand specimens under rapid and dynamic loading. *Int. J. Numer. Anal. Met.*, 31(6):757–788, 2007.

[29] Z. Ding, F. Romanelli, Y. Chen, and G. Panza. Realistic modeling of seismic wave ground motion in Beijing city. *Pure Appl. Geophys.*, 161(5-6):1093–1106, 2004.

[30] J. Douglas and H. Aochi. A survey of techniques for predicting earthquake ground motions for engineering purposes. *Surv. Geophys.*, 29(3):187, 2008.

[31] J. Douglas and B. Edwards. Recent and future developments in earthquake ground motion estimation. *Earth-Science Reviews*, 160:203–219, 2016.

[32] B. R. Ellingwood. Earthquake risk assessment of building structures. *Reliab. Eng. Syst. Safe.*, 74(3):251–262, 2001.

[33] Y. Epshteyn and B. Rivière. Estimation of penalty parameters for symmetric interior penalty Galerkin methods. *J. Comput. Appl. Math.*, 206(2):843–872, 2007.

[34] M. Erdik. Earthquake risk assessment. *B. Earthq. Eng.*, 15(12):5055–5092, 2017.

[35] L. Evangelista, S. del Gaudio, C. Smerzini, A. d'Onofrio, G. Festa, I. Iervolino, L. Landolfi, R. Paolucci, A. Santo, and F. Silvestri. Physics-based seismic input for engineering applications: a case study in the Aterno river valley, Central Italy. *B. Earthq. Eng.*, 15(7):2645–2671, 2017.

[36] E. Faccioli, F. Maggio, R. Paolucci, and A. Quarteroni. 2D and 3D elastic wave propagation by a pseudo-spectral domain decomposition method. *J. Seismol.*, 1(3):237–251, 1997.

[37] M. Gao, Y. Yu, X. Zhang, and J. Wu. Three-dimensional finite-difference modeling of ground motions in Beijing form a Mw 7 scenario earthquake. In *Proceedings of the 13th World Conference on Earthquake Engineering*. Paper 581, 2004.

[38] B. Gencturk, A. S. Elnashai, and J. Song. Fragility relationships for populations of woodframe structures based on inelastic response. *J. Earthq. Eng.*, 12(S2):119–128, 2008.

[39] R. Graves, T. Jordan, S. Callaghan, E. Deelman, E. Field, G. Juve, C. Kesselman, P. Maechling, G. Mehta, K. Milner, D. Okaya, P. Small, and K. Vahi. CyberShake: A physics-based seismic hazard model for Southern California. *Pure and Applied Geophysics*, 168(3-4):367–381, 2011.

[40] R. W. Graves. Simulating seismic wave propagation in 3D elastic media using staggered-grid finite differences. *B. Seismol. Soc. Am.*, 86(4):1091–1106, 1996.

[41] G. Gu, T. Lin, and Z. Shi. Catalogue of earthquakes in China (1831AD–1969BC). *Science Press, Beijing (in Chinese)*, 1983.

[42] R. Guidotti, M. Stupazzini, C. Smerzini, R. Paolucci, and P. Ramieri. Numerical study on the role of basin geometry and kinematic seismic source in 3D ground motion simulation of the 22 February 2011 Mw 6.2 Christchurch earthquake. *Seismological Research Letters*, 82(6):767–782, 2011.

[43] C. He, Q. Huang, Y. Dou, W. Tu, and J. Liu. The population in China's earthquake-prone areas has increased by over 32 million along with rapid urbanization. *Environ. Res. Lett.*, 11(7):074028, 2016.

[44] M. Infantino, I. Mazzieri, A. Özcebe, R. Paolucci, and M. Stupazzini. Physics-based probabilistic seismic hazard assessment in Istanbul, Part 1: 3D numerical modelling and simulated earthquake ground motions. *submitted*, 2019.

[45] N. Jayaram and J. Baker. Correlation model for spatially distributed ground-motion intensities. *Earthquake Engineering and Structural Dynamics*, 38(15):1687–1708, 2009.

[46] S.-H. Jeong, A. M. Mwafy, and A. S. Elnashai. Probabilistic seismic performance assessment of code-compliant multi-story RC buildings. *Eng. Struct.*, 34:527–537, 2012.

[47] M. Käser and M. Dumbser. An arbitrary high-order discontinuous Galerkin method for elastic waves on unstructured meshes–I. The two-dimensional isotropic case with external source terms. *Geophys. J. Int.*, 166(2):855–877, 2006.

[48] A. Kazantzi, D. Vamvatsikos, K. Porter, and I. H. Cho. Analytical vulnerability assessment of modern highrise RC moment-resisting frame buildings in the Western USA for the Global Earthquake Model. In *Proceedings of the 2nd European Conference on Earthquake Engineering and Seismology*, 2014.

[49] D. Komatitsch and J.-P. Vilotte. The spectral element method: an efficient tool to simulate the seismic response of 2D and 3D geological structures. *B. Seismol. Soc. Am.*, 88(2):368–392, 1998.

[50] S. Kramer. Earthquake geotechnical engineering, 1996.

[51] X. Lu, X. Zeng, Z. Xu, and H. Guan. Improving the accuracy of near real-time seismic loss estimation using post-earthquake remote sensing images. *Earthq. Spectra*, 34(3):1219–1245, 2019.

[52] N. Luco and C. Cornell. Structure-specific scalar intensity measures for near-source and ordinary earthquake ground motions. *Earthq. Spectra*, 23(2):357–392, 2007.

[53] J. Lysmer and L. A. Drake. A finite element method for seismology. In *Seismology: Surface Waves and Earth Oscillations*, volume 11 of *Methods in Computational Physics: Advances in Research and Applications*, pages 181–216. Academic Press Inc, 1972.

[54] C. Mai, K. Konakli, and B. Sudret. Seismic fragility curves for structures using non-parametric representations. *Front. Struct. Civ. Eng.*, 11(2):169–186, 2017.

[55] I. Mazzieri, M. Stupazzini, R. Guidotti, and C. Smerzini. SPEED: SPectral Elements in Elastodynamics with Discontinuous Galerkin: a non-conforming approach for 3D multi-scale problems. *Internat. J. Numer. Methods Engrg.*, 95(12):991–1010, 2013.

[56] J. Moehle, Y. Bozorgnia, N. Jayaram, P. Jones, M. Rahnama, N. Shome, Z. Tuna, J. Wallace, T. Yang, and F. Zareian. Case studies of the seismic performance of tall buildings designed by alternative means. *Pacific Earthquake Engineering Research Center College of Engineering University of California, Berkeley PEER Report*, 5, 2011.

[57] R. Paolucci, L. Evangelista, I. Mazzieri, and E. Schiappapietra. The 3D numerical simulation of near-source ground motion during the Marsica earthquake, Central Italy, 100 years later. *Soil Dynamics and Earthquake Engineering*, 91:39–52, 2016.

[58] R. Paolucci, M. Infantino, I. Mazzieri, A. G. Özcebe, C. Smerzini, and M. Stupazzini. 3D physics-based numerical simulations: advantages and current limitations of a new frontier to earthquake ground motion prediction. The Istanbul case study. In *Recent Advances in Earthquake Engineering in Europe: 16th European Conference on Earthquake Engineering-Thessaloniki 2018*, pages 203–223. Springer, 2018.

[59] R. Paolucci, I. Mazzieri, and C. Smerzini. Anatomy of strong ground motion: Near-source records and three-dimensional physics-based numerical simulations of the Mw 6.0 2012 May 29 Po plain earthquake, Italy. *Geophys. J. Int.*, 203(3):2001–2020, 2015.

[60] R. Paolucci, I. Mazzieri, C. Smerzini, and M. Stupazzini. Physics-based earthquake ground shaking scenarios in large urban areas. In *Perspectives on European earthquake engineering and seismology*, pages 331–359. Springer, 2014.

[61] J. Park, P. Bazzurro, and J. Baker. Modeling spatial correlation of ground motion intensity measures for regional seismic hazard and portfolio loss estimation. In *Applications of Statistics and Probability in Civil Engineering - Proceedings of the 10th International Conference on Applications of Statistics and Probability, ICASP10*, 2007.

[62] I. Peruš and P. Fajfar. How reliable are the ground motion prediction equations. In *Proceedings of the 20th International Conference on Structural Mechanics in Reactor Technology (SMiRT 20), Espoo*, volume 9. Paper 1662, 2009.

[63] K. Porter, L. Jones, D. Cox, J. Goltz, K. Hudnut, D. Mileti, S. Perry, D. Ponti, M. Reichle, A. Rose, C. Scawthorn, H. Seligson, K. Shoaf, J. Treiman, and A. Wein. The ShakeOut scenario: A hypothetical Mw7.8 earthquake on the Southern San Andreas fault. *Earthq. Spectra*, 27(2):239–261, 2011.

[64] K. Porter, R. Kennedy, and R. Bachman. Creating fragility functions for performance-based earthquake engineering. *Earthq. Spectra*, 23(2):471–489, 2007.

[65] A. Quarteroni and A. Valli. *Numerical approximation of partial differential equations*, volume 23 of *Springer Series in Computational Mathematics*. Springer-Verlag, Berlin, 1994.

[66] A. Quilligan, A. O'Connor, and V. Pakrashi. Fragility analysis of steel and concrete wind turbine towers. *Eng. Struct.*, 36:270–282, 2012.

[67] B. Rivière, S. Shaw, and J. R. Whiteman. Discontinuous Galerkin finite element methods for dynamic linear solid viscoelasticity problems. *Numer. Methods Partial Differential Equations*, 23(5):1149–1166, 2007.

[68] B. Rivière and M. F. Wheeler. Discontinuous finite element methods for acoustic and elastic wave problems. In *Current trends in scientific computing (Xi'an, 2002)*, volume 329 of *Contemp. Math.*, pages 271–282. Amer. Math. Soc., Providence, RI, 2003.

[69] T. Rossetto and A. Elnashai. Derivation of vulnerability functions for European-type RC structures based on observational data. *Eng. Struct.*, 25(10):1241–1263, 2003.

[70] T. Rossetto and A. Elnashai. A new analytical procedure for the derivation of displacement-based vulnerability curves for populations of RC structures. *Eng. Struct.*, 27(3):397–409, 2005.

[71] M. Rota, A. Penna, and G. Magenes. A methodology for deriving analytical fragility curves for masonry buildings based on stochastic nonlinear analyses. *Eng. Struct.*, 32(5):1312–1323, 2010.

[72] D. Seyedi, P. Gehl, J. Douglas, L. Davenne, N. Mezher, and S. Ghavamian. Development of seismic fragility surfaces for reinforced concrete buildings by means of nonlinear time-history analysis. *Earthq. Eng. Struct. D.*, 39(1):91–108, 2010.

[73] M. Shinozuka, M. Q. Feng, J. Lee, and T. Naganuma. Statistical analysis of fragility curves. *J. Eng. Mech.*, 126(12):1224–1231, 2000.

[74] A. Singhal and A. S. Kiremidjian. Method for probabilistic evaluation of seismic structural damage. *J. Struct. Eng.*, 122(12):1459–1467, 1996.

[75] C. Smerzini and K. Pitilakis. Seismic risk assessment at urban scale from 3D physics-based numerical modeling: the case of Thessaloniki. *B. Earthq. Eng.*, 16(7):2609–2631, 2018.

[76] C. Smerzini, K. Pitilakis, and K. Hashemi. Evaluation of earthquake ground motion and site effects in the Thessaloniki urban area by 3D finite-fault numerical simulations. *B. Earthq. Eng.*, 15(3):787–812, 2017.

[77] A. Smolka, A. Allmann, D. Hollnack, and H. Thrainsson. The principle of risk partnership and the role of insurance in risk mitigation. In *Proceedings of the 13th World Conference on Earthquake Engineering*. Paper 2020, 2004.

[78] R. Stacey. Improved transparent boundary formulations for the elastic-wave equation. *B. Seismol. Soc. Am.*, 78(6):2089–2097, 1988.

[79] M. Stupazzini, M. Infantino, A. Allmann, and R. Paolucci. Physics-based probabilistic seismic hazard assessment in Istanbul, Part 2: hazard and loss estimates. *submitted*, 2019.

[80] M. Stupazzini, R. Paolucci, and H. Igel. Near-fault earthquake ground-motion simulation in the Grenoble valley by a high-performance spectral element code. *Bull. seism. Soc. Am.*, 99(1):286–301, 2009.

[81] M. Villani, E. Faccioli, M. Ordaz, and M. Stupazzini. High resolution seismic hazard analysis in a complex geological configuration: The case of the Sulmona basin in Central Italy. *Earthq. Spectra*, 30(4):1801–1824, 2014.

[82] M. Vona. Fragility curves of existing RC buildings based on specific structural performance levels. *Open Journal of Civil Engineering*, 4(02):120, 2014.

[83] G. Weatherill, V. Silva, H. Crowley, and P. Bazzurro. Exploring the impact of spatial correlations and uncertainties for portfolio analysis in probabilistic seismic loss estimation. *B. Earthq. Eng.*, 13(4):957–981, 2015.

[84] F. Wu, M. Wang, and X. Y. Yang. Building seismic vulnerability study for China high rises. *Appl. Mech. Mater.*, 353:2301–2304, 2013.

[85] H. Xiansheng and G. Yanping. An example of seismic risk analysis in Beijing. *Proceedings of the 9th World Conference on Earthquake Engineering*, II, 1988.

[86] F. Xie, Z. Wang, and J. Liu. Seismic hazard and risk assessments for Beijing-Tianjin-Tangshan, China, area. *Pure Appl. Geophys.*, 168(3-4):731–738, 2011.

[87] D. Xin, J. E. Daniell, and F. Wenzel. State of the art of fragility analysis for major building types in China with implications for intensity-PGA relationships. *Nat. Hazards Earth Syst. Sci. Discuss.*, 2018.

[88] C. Xiong, X. Lu, J. Huang, and H. Guan. Multi-LOD seismic-damage simulation of urban buildings and case study in Beijing CBD. *B. Earthq. Eng.*, 17(4):2037–2057, 2019.

[89] P. Xu, C. Xiao, and J. Li. Relationship between natural vibration periods and structural heights for high-rise buildings in China. *International Journal of High-rise Buildings*, 3(1):49–64, 2014.

[90] Z. Xu, X. Lu, X. Zeng, Y. Xu, and Y. Li. Seismic loss assessment for buildings with various-LOD BIM data. *Adv. Eng. Inform.*, 39:112–126, 2019.

[91] I. Zentner. Numerical computation of fragility curves for NPP equipment. *Nucl. Eng. Des.*, 240(6):1614–1621, 2010.

MOX Technical Reports, last issues

Dipartimento di Matematica
Politecnico di Milano, Via Bonardi 9 - 20133 Milano (Italy)

33/2019 Regazzoni, F.; Dede', L.; Quarteroni, A.
Machine learning of multiscale active force generation models for the efficient simulation of cardiac electromechanics

31/2019 Pagani, S.; Vitulano, G.; De Blasi, G.; Frontera, A.
High density characterization of the atrial electrical substrate during sinus rhythm in patients with atrial fibrillation

32/2019 Fedele, M.
Polygonal surface processing and mesh generation tools for numerical simulations of the complete cardiac function.

30/2019 Pagani, S.; Manzoni, A.; Quarteroni, A.
Forward uncertainty quantification in cardiac electrophysiology by reduced order modeling and machine learning

29/2019 Dal Santo, N.; Manzoni, A.; Pagani, S.; Quarteroni, A.
Reduced order modeling for applications to the cardiovascular system

28/2019 Infantino, M.; Mazzieri, I.; Ozcebe, A.G.; Paolucci, R.; Stupazzini, M.
Physics-based probabilistic seismic hazard assessment in Istanbul

26/2019 Antonietti, P. F.; Bonaldi, F.; Mazzieri, I.
Simulation of 3D elasto-acoustic wave propagation based on a Discontinuous Galerkin Spectral Element method

27/2019 Tantardini, M.; Ieva, F.; Tajoli, L.; Piccardi, C.
Comparing methods for comparing networks

25/2019 Gigante, G.; Vergara, C.
On the stability of a loosely-coupled scheme based on a Robin interface condition for fluid-structure interaction

24/2019 Masci, C.; Ieva, F.; Agasisti, T.; Paganoni A.M.
Evaluating class and school effects on the joint achievements in different subjects: a bivariate semi-parametric mixed-effects model